Three-dimensional micromagnetic simulations of multidomain bubble-state excitation spectrum in ferromagnetic cylindrical nanodots

N. Vukadinovic*
Dassault Aviation, 78 quai Marcel Dassault, 92 552 St-Cloud, France

F. Boust
Onera, Chemin de la Hunière, 91761 Palaiseau, France

(Received 18 July 2008; revised manuscript received 6 October 2008; published 13 November 2008)

The excitation spectrum of multidomain bubble states in cylindrical nanodots with a large perpendicular anisotropy has been investigated by means of three-dimensional micromagnetic simulations for various dot diameters. In a first step, the evolution of the zero-field susceptibility spectra as a function of the dot diameter is studied for bidomain bubble states. Increasing dot diameter leads to shifts of the resonance frequencies toward the low frequencies for the fundamental domain wall and domain modes, whereas the spectral positions of surface domain wall and domain modes are weakly affected. Second, the high-frequency response of a tridomain bubble state stabilized in larger dot diameters is analyzed. Dynamic interaction effects are revealed mainly through the identification of coupled domain-wall modes, the resonance frequencies of which depend on the relative domain-wall chiralities. Lastly, the magnetization dynamics of a metastable bidomain bubble state with a pair of vertical Bloch lines, each of them possessing a Bloch point, is addressed. In such a case, the presence of magnetic singularities leads to a splitting of the fundamental domain-wall mode into two resonance lines assigned to oscillations of domain-wall parts with different phase relations.

DOI: 10.1103/PhysRevB.78.184411 PACS number(s): 75.40.Gb, 75.40.Mg, 75.75.+a

I. INTRODUCTION

Mesoscopic magnetic elements with a uniaxial perpendicular anisotropy are nowadays the subject of considerable attention. Besides the potential applications in high-density storage media and magnetoelectronic devices, these magnetic objects can be viewed, from the theoretical point of view, as a model system for studying the spin dynamics within confined geometries with well-controlled equilibrium magnetization configurations. Indeed, a remarkable feature of such objects is the ability to display a large variety of stable remanent micromagnetic states depending on the system shape and size, the strength of the perpendicular anisotropy characterized by the quality factor Q ($Q=2K_u/\mu_0 M_S^2$, where K_u is the uniaxial perpendicular anisotropy, M_S the saturation magnetization, and μ_0 the permeability of free space), and the magnetic history of the sample.

A significative effort has been devoted to the static magnetic properties of such elements mainly in terms of observation and analysis of stable micromagnetic states.[1–9] Pioneer experimental works on submicrometer-size hcp Co dots revealed, in particular, the presence of concentric domains above a critical dot thickness[1] by means of magnetic force microscopy (MFM) images. The concentric domains consist in coaxial domains with alternately up and down perpendicular magnetization components, the domains adopting the in-plane shape of the magnetic element.[4] This magnetic configuration recalls the weak stripe domain structure existing in extended films with a perpendicular anisotropy.[10] For cylindrical Co dots, the stability range for concentric weak stripe domains in the plane (thickness, diameter) has been estimated by means of static micromagnetic simulations.[5] Similarly, it has been evidenced[6] by combining MFM images and static micromagnetic simulations that Ni dots support various regular domain patterns, the characteristics of which can be predicted by the reduced parameter $D_0=D/P_0$, where D is the dot diameter and P_0 is the zero-field period of stripe domains existing for the continuous film with the same magnetic parameters and the same thickness.[10–12] The quasiuniform single-domain flower state is the only stable configuration for $D_0<1/2$, whereas bidomain states appear energetically favorable for larger values of D_0 ($D_0 \simeq 1$). Two types of bidomain states have been identified, namely, a two-stripe domain structure including a rectilinear domain wall (DW) and a concentric bidomain state. A detailed analysis of the equilibrium magnetization associated with concentric bidomain states has been performed for low ($Q \ll 1$, Permalloy-like systems) and moderate ($Q<1$, Co- or Ni-like systems) Q factors.[7] The case of large Q factor ($Q>1$, FePt-like systems) has been also recently reported.[8,9] The concentric bidomain structure was found to be the ground state for cylindrical dots within a large diameter range. For this Q value regime, the concentric bidomain state displays up and down circular domains separated by a sharp DW and can be viewed as the confined version of a bubble domain existing in a perpendicular magnetized film.[13] Hereafter, this magnetic configuration will be termed bidomain bubble state. The stability of the bidomain bubble state as functions of the dot diameter, the dot thickness, and the strength of a static magnetic field applied along the symmetry axis has been also studied numerically.[8]

On the other hand, the dynamic properties of such objects have been far less investigated. Recently, the high-frequency (0.1–80 GHz) linear response of cylindrical elements with a large perpendicular anisotropy supporting bidomain states ($D_0 \simeq 1$) has been investigated using three-dimensional (3D) micromagnetic simulations.[14] For both the two-stripe domain and the bidomain bubble states, it has been found that the

zero-field dynamic susceptibility spectra exhibit multiple resonance lines assigned to domain-wall modes, mixed domain wall and domain modes, and domain modes. However, the magnetic excitation spectrum for higher lateral size elements remains to be explored.

The present work has been also partly motivated by recent experimental results that evidenced the presence of single (bidomain) and higher-order (tridomain) magnetic bubbles in FePt dots with various diameters by MFM imaging.[9] In addition, a phase diagram in the plane (radius and thickness) was numerically constructed, delimiting the stability range for theses two states.

The main purpose of this paper is to investigate the static and dynamic properties of bubble states as a function of the dot diameter by means of full 3D micromagnetic simulations. In a first part, the range $1 \leq D_0 \leq 2$, where the bidomain bubble state is energetically favorable, is probed. The dot diameter dependence of the associated dynamic susceptibility spectra is pointed out. In the second part, the tridomain bubble state ($D_0 \simeq 2$) is considered. Attention is paid on the dynamic coupling between the two DWs inside the cylindrical dot. In addition, the role played by the relative chiralities of the DWs on the high-frequency response of the tridomain bubbles is analyzed. Lastly, the complicated case of a metastable bidomain bubble state—including a pair of interacting vertical Bloch lines (VBLs), each of them possessing a Bloch point (BP)—is investigated. The presence of such magnetic singularities affects deeply the dynamic susceptibility spectra with the splitting of the fundamental DW mode. Resonant absorptions arising from DW parts are thereby identified.

II. NUMERICAL METHOD AND SAMPLE CHARACTERISTICS

The high-frequency response of multidomain bubble states is investigated by means of micromagnetic simulations using two 3D codes described elsewhere.[15] These codes are based on the Landau-Lifshitz (LL) equation for magnetization motion,

$$\frac{d\mathbf{M}(\mathbf{r},t)}{dt} = -\mu_0|\gamma|\left\{\mathbf{M}(\mathbf{r},t)\times\mathbf{H}_{\text{eff}}(\mathbf{r},t)+\frac{\alpha}{M_S}\mathbf{M}(\mathbf{r},t)\times[\mathbf{M}(\mathbf{r},t)\times\mathbf{H}_{\text{eff}}(\mathbf{r},t)]\right\}, \quad (1)$$

where $\mathbf{M}(\mathbf{r},t)$ is the magnetization vector which depends both on space and time, γ is the gyromagnetic ratio, and α is the damping parameter. The effective field $\mathbf{H}_{\text{eff}}(\mathbf{r},t)$ incorporates the contributions from exchange, anisotropy, demagnetizing, and applied magnetic fields. The first code computes an equilibrium magnetization configuration by integrating the LL equation in the time domain using a second-order Taylor scheme and an optimized time step. The second one computes the full susceptibility tensor $\bar{\chi}$, which relates the high-frequency response of a magnetic configuration $\delta\mathbf{m}$ to a weak radio frequency (rf) magnetic exciting field $\delta\mathbf{h}$ such as $\delta\mathbf{m}=\bar{\chi}\delta\mathbf{h}$. The method is based on the linearization of the LL equation around the equilibrium magnetization configuration (small-amplitude motion regime). For this purpose, the magnetization vector and the effective field are written as the sum of a static part and a small dynamic perturbation. Restricting to the first-order terms for the dynamic perturbations in Eq. (1) and assuming an harmonic time dependence for both $\delta\mathbf{h}$ and $\delta\mathbf{m}$, the LL equation is then transformed into the following linear system:

$$\left(-\frac{i\omega}{\mu_0|\gamma|M_S}I+D_2-D_1D_H\right)\delta\mathbf{m}=D_1\delta\mathbf{h}, \quad (2)$$

where I is the unit operator and D_H, D_1, and D_2 are linear operators defined in Ref. 15 (these expressions differ for the Landau-Lifshitz-Gilbert equation[16]). For a given pumping field $\delta\mathbf{h}$ and a given angular frequency ω, the solution of the linear system [Eq. (2)] gives access to the dynamic magnetization $\delta\mathbf{m}(\mathbf{r},\omega)$. By considering an orthogonal basis of unitary excitation vectors $(\delta\mathbf{h}_1,\delta\mathbf{h}_2,\delta\mathbf{h}_3)$ and the resulting responses $(\delta\mathbf{m}_1,\delta\mathbf{m}_2,\delta\mathbf{m}_3)$, the local dynamic susceptibility tensor is given by

$$\chi_{ij}(\mathbf{r},\omega)=\delta\mathbf{m}_i\cdot\delta\mathbf{h}_j \quad i,j=1,2,3, \quad (3)$$

and the dynamic susceptibility tensor averaged over the particle's volume V is expressed by

$$\chi_{ij}(\omega)=\langle\chi_{ij}(\mathbf{r},\omega)\rangle_V \quad i,j=1,2,3. \quad (4)$$

These two quantities will be exploited hereafter. The local susceptibility tensor allows visualizing the spatial distribution of the high-frequency magnetic response within the particle and especially at the resonance frequencies of absorption lines. For axially symmetric elements, the map of local susceptibility will be displayed in a vertical plane cutting the dot center. The frequency-dependent global susceptibility tensor corresponds to the dynamic susceptibility spectrum. Hereafter, the analysis will be restricted to the imaginary parts of diagonal elements of local and global susceptibility tensors, and only spatially uniform pumping fields will be considered. It should be stressed that one advantage of this frequency domain method is the possibility of spectral refinement around the absorption lines ensuring high-resolution spectra. Typically, between 100 and 200 frequency points were necessary for obtaining each susceptibility spectrum presented in Sec. III.

In order to solve the linear system [Eq. (2)], the magnetic sample is discretized using a regular cubic mesh. The mesh sizes Δ_i, $i=x,y,z$ are chosen to be lower than the smallest characteristic length between the exchange length, $\Lambda=\sqrt{2A/(\mu_0 M_s^2)}$, where A is the exchange constant and the Bloch DW width parameter Δ_0 is defined as $\Delta_0=\sqrt{A/K_u}$. These static and dynamic micromagnetic codes were previously used for studying the high-frequency response of small Py cylindrical dots with a vortex-type magnetic configuration[17] and cylindrical dots with a perpendicular anisotropy supporting bidomain states.[14]

The micromagnetic simulations were performed using magnetic parameters representative of ferromagnetic alloys (FePt, CoPt, and FePd) displaying a large perpendicular anisotropy ($Q>1$) and similar to those reported in Ref. 14, namely: $M_S=1.12510^6$ A/m, $A=10^{-11}$ J/m, $K_u=0.9510^6$

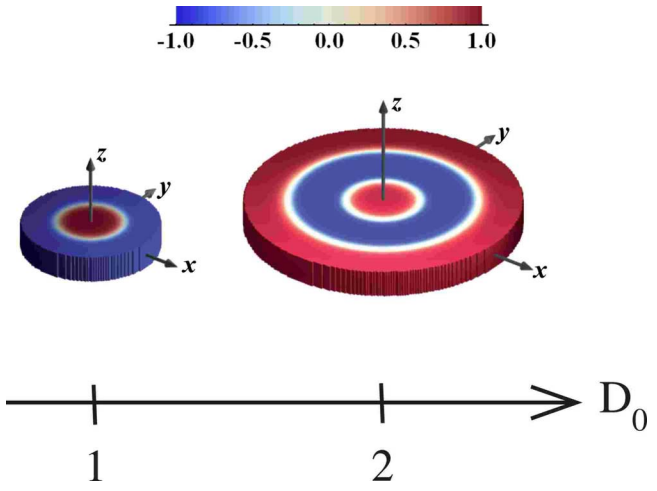

FIG. 1. (Color online) Bidomain and tridomain bubble states for a cylindrical dot with $Q=1.2$, $L_z=19.2$ nm. The dot diameter corresponds to $D=96$ nm ($D_0 \simeq 1$, with $D_0=D/P_0$, and P_0 is the zero-field stripe period of the extended film) for the bidomain bubble state (left image) and $D=192$ nm ($D_0 \simeq 2$) for the tridomain bubble state (right image). The color images represent the reduced magnetization component $m_z=M_z/M_S$ at the dot boundaries for the respective bubble states.

J/m^3, the gyromagnetic ratio $\gamma=1.7610^{11}$ s^{-1} T^{-1}, and the damping parameter $\alpha=0.02$. The quality factor Q is equal to 1.2. The corresponding characteristic lengths are $\Lambda=3.5$ nm and $\Delta_0=3.2$ nm, and the mesh sizes were chosen to be equal to $\Delta_x=\Delta_y=\Delta_z=1.2$ nm. Two dot thicknesses are considered $L_z=19.2$ nm for the first two parts and $L_z=38.4$ nm for the last one [bidomain bubble configuration with Bloch lines (BLs)], whereas the dot diameter ranges from $D=96$ nm ($D_0 \simeq 1$) up to $D=192$ nm ($D_0 \simeq 2$). It should be remarked that reducing dot thickness with respect to the Ref. 14 leads to a small decrease in the zero-field stripe period (about 10 % between $L_z=50$ nm and $L_z=19.2$ nm) and, consequently, does not change significantly the value of D_0.

III. MICROMAGNETIC SIMULATION RESULTS

A. Bidomain bubble state

This section addresses the bidomain bubble configuration in the range $1 \leq D_0 \leq 2$. The computed static magnetization configuration of the bidomain bubble state at remanence is illustrated in Fig. 1 (upper left image), which represents the reduced magnetization component $m_z=M_z/M_S$ at the dot boundaries for a cylindrical dot with $D=96$ nm and $L_z=19.2$ nm. The inner domain is upward magnetized, whereas the outer domain is downward magnetized. Detailed descriptions of the magnetization configuration associated with the bidomain bubble state have been previously reported.[8,9,14] In short, the main characteristics are the following. (i) At remanence, the bidomain bubble state has a nonzero total magnetization along the symmetry axis, the size of the inner domain being lower than the one of the outer domain. (ii) The circular DW is twisted with a Bloch

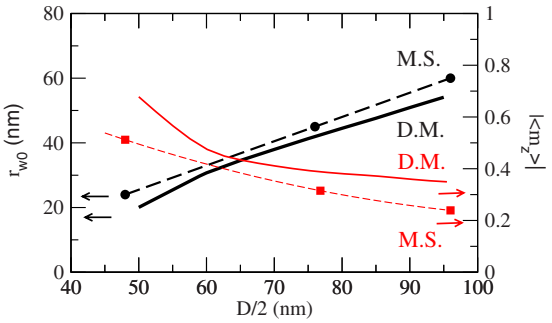

FIG. 2. (Color online) Evolutions of the equilibrium DW radius r_{w0} (black lines and symbols) and the net perpendicular magnetization component $|\langle m_z \rangle|$ (red lines and symbols) as a function of the dot radius. The results of 3D micromagnetic simulations are displayed using full circles (r_{w0}) and squares ($|\langle m_z \rangle|$). For the micromagnetic simulations, the equilibrium DW radius is evaluated at the midplane of the dot $z=0$. The dashed curves are guides for eyes. The solid curves represent the dot radius dependences of r_{w0} and $|\langle m_z \rangle|$ deduced from the analytical domain model [Eq. (7)].

character at the dot center and a Néel character at the dot surfaces, the Néel part being wider than the Bloch part. (iii) The domain magnetization deviates slightly from the z axis at the dot edge (flowering effect). Increasing dot diameter leads to an expansion of the DW. The DW radius at the midplane of the dot, $z=0$, varies linearly with the dot diameter as reported in Fig. 2. Consequently, the absolute value of the space-averaged reduced magnetization along the z axis, $|\langle m_z \rangle|$, is reduced for increasing dot diameter. It is instructive to compare these variations computed by micromagnetic simulations with the ones deduced from an analytical domain model valid in the high-Q limit. This model is based on the assumptions of alternately up and down domains separated by an infinitely thin cylindrical DW characterized by the surface energy density σ_w and the radius r_w. In addition, the z dependence of the magnetization configuration is neglected (in particular, no DW twist). This approach was first developed for studying the stability of magnetic bubbles within an infinite plate.[18] Later, the effect of the finite extent of a circular plate was incorporated in the model.[19] In our case, the equilibrium DW radius, r_{w0}, results from the balance between the pressures on the DW originating from the surface tension and the demagnetizing field. This condition reads:

$$\frac{\sigma_w}{r_w} = 2M_S \bar{H}_{D,z}(r_w), \tag{5}$$

where $\bar{H}_{D,z}(r_w)$ is the z component of the demagnetizing field averaged over the dot thickness, evaluated at the DW radius, $\bar{H}_{D,z}(r_w)=\frac{1}{L_z}\int_0^{L_z} H_{z,D}(z,r_w)dz$. $\bar{H}_{D,z}$ can be computed using the superposition of the demagnetizing fields arising from two uniformly magnetized cylinders with magnetization $M_z=-M_S$ and radius r (dot radius), and magnetization $M_z=+2M_S$ and radius r_w, respectively.[20] This leads to the following expression:

$$\bar{H}_{D,z} = -\mu_0 M_S \left\{ \frac{2r_w}{L_z}\left[F_1(1,0) - F_1\left(1,\frac{L_z}{r_w}\right)\right] - \frac{r}{L_z}\left[F_1\left(\frac{r}{r_w},0\right) - F_1\left(\frac{r}{r_w},\frac{L_z}{r_w}\right)\right]\right\}, \quad (6)$$

where the F_1 function is defined as[21] $F_1(a,b) = \int_0^\infty e^{-bu} J_0(u) J_1(au) \frac{du}{u}$ with J_0 and J_1 the Bessel functions of the zero and first orders.

Inserting Eq. (6) in Eq. (5), the z-averaged force equation takes, therefore, the following form:

$$\frac{l}{L_z} + \frac{2r_w}{L_z}\left\{ \frac{2r_w}{L_z}\left[F_1(1,0) - F_1\left(1,\frac{L_z}{r_w}\right)\right] - \frac{r}{L_z}\left[F_1\left(\frac{r}{r_w},0\right) - F_1\left(\frac{r}{r_w},\frac{L_z}{r_w}\right)\right]\right\} = 0, \quad (7)$$

with $l \equiv \sigma_w / \mu_0 M_S^2 = 4\sqrt{AK_u}/\mu_0 M_S^2$. Solving Eq. (7) for fixed values of dot radius $r=D/2$, l, and L_z gives access to r_{w0} and then to $\langle m_z \rangle = 2r_{w0}^2/r^2 - 1$. As shown in Fig. 2, the domain model reproduces fair satisfactorily the evolutions of r_{w0} and $|\langle m_z \rangle|$ as a function of the dot radius found by micromagnetic simulations.

The dynamic susceptibility spectra of a cylindrical dot ($D=96$ nm and $L_z=48$ nm) supporting a bidomain bubble state have been previously investigated.[14] As a result, the imaginary parts of the longitudinal susceptibility spectrum χ''_{zz} and the transverse ones expressed in terms of circular elements $\chi''_{\pm}$, with $\chi_{\pm} = \chi_{xx} \pm j\chi_{xy}$, have revealed up to 16 resonance lines within the frequency range 0.1–80 GHz. These resonance lines arise from DW modes, mixed DW and domain modes, and domain modes. In order to keep reasonable computational times and to allow varying the dot diameter, the cylindrical dot reported in Fig. 1 with the same diameter $D=96$ nm but with a thickness $L_z=19.2$ nm is considered as the reference case for the bidomain bubble state in the present article. By comparison with the results obtained in Ref. 14, it appears that decreasing dot thickness results in a reduced number of resonance lines. For the sake of clarity, only the longitudinal and the predominant circular susceptibility spectra will be presented hereafter. Figure 3(a) shows three resonance lines situated at 7.29, 24.96, and 40 GHz for the χ''_- spectrum and one intensive peak at 5.38 GHz followed by a very weak one at 24.62 GHz for the χ''_{zz}. The maps of the local susceptibility associated with these five resonance lines are represented in Fig. 3(b) using a vertical slice at $y=0$. Resonance line 1 corresponds to a strongly nonuniform mode concentrated at the lateral sides of the DW. Resonance line 2 results from a surface mode localized near the DW (down domain side). Resonance line 3 arises from spins in the outer down domain. This mode is quasiuniform along the z axis. A similar mode localized in the inner up domain exists also for the χ''_+ spectrum (not presented here). It should be noted that the small dot thickness prevents the splitting of the domain mode into surface and core modes as observed in Ref. 14 (modes 5 and 7 in Fig. 5). For the χ''_{zz} spectrum, the predominant peak 4 is a DW mode quasiuniform along the z axis, whereas the weak signal 5 is assigned to a DW mode preferentially localized near the dot

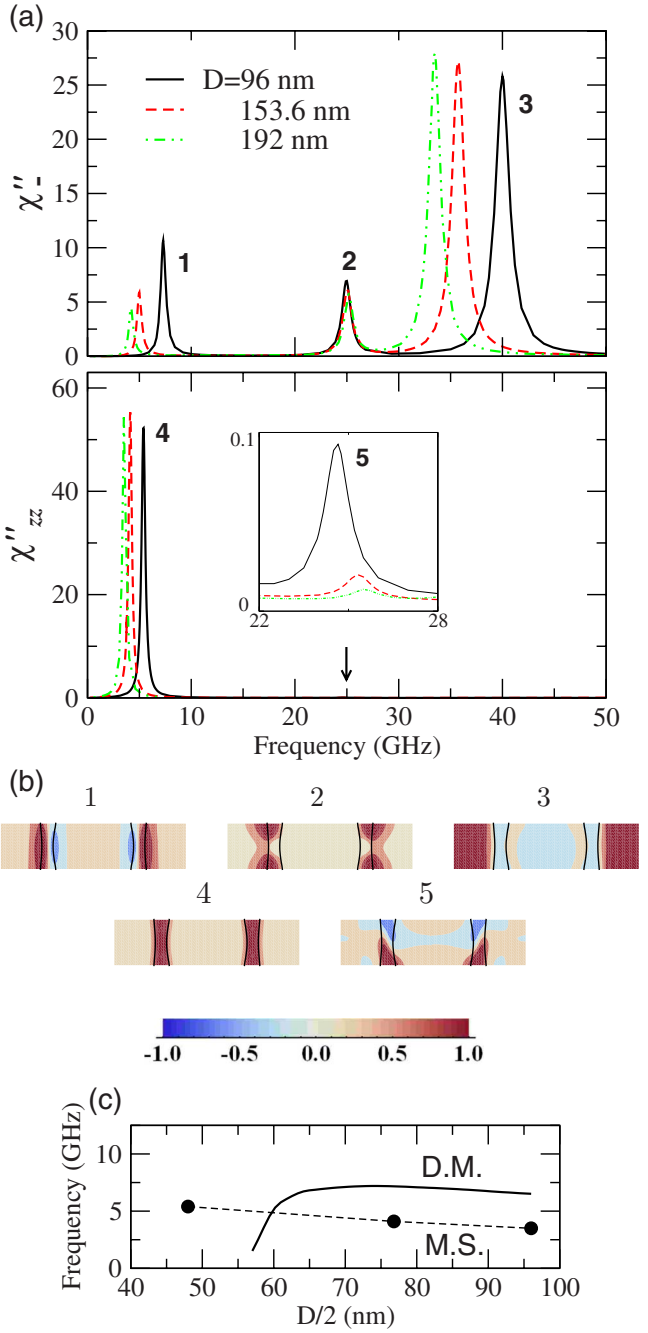

FIG. 3. (Color online) High-frequency response of bidomain bubble states as a function of the dot diameter for a fixed dot thickness $L_z=19.2$ nm. (a) Zero-field dynamic susceptibility spectra for the predominant circular transverse element χ''_- and the longitudinal element χ''_{zz}. Three dot diameters are considered: $D=96$ nm (black solid line), $D=153.6$ nm (red dashed line), and $D=192$ nm (green dot-dashed line). (b) Cross-sectional view of the local dynamic susceptibility in the vertical plane $y=0$ at the resonance frequency of different lines for the dot with $D=96$ nm. The color code represents the local susceptibility (imaginary part) normalized by its maximum value (absolute value). (c) Evolutions of the resonance frequency for the fundamental DW mode (resonance line 4) computed from micromagnetic simulations (full circles) and the domain model (solid line). The dashed curve is a guide for eyes.

surfaces. With respect to the spectra reported in Ref. 14, reducing dot thickness leads to a shift of the spectral positions for the surface modes (resonance lines 2 and 5) toward the higher frequencies. For DW mode 5, this change in resonance frequency is accompanied with a strong attenuation of the line. This behavior is consistent with the ones observed for the Néel-type excitation in thin films with perpendicular anisotropy,[22] and for higher-order vortex core modes existing in cylindrical dots[17] and prismatic elements without perpendicular anisotropy.[23]

Next, the effect of the dot diameter on the dynamic susceptibility spectra is analyzed. For the probed size regime, the number of peaks remains constant when changing dot diameter. Figure 3(a) reveals that the resonance frequencies of lines 1, 3, and 4 are monotonously lowered for increasing dot diameter, whereas the spectral position of line 2 is weakly affected (small increase in the resonance frequency with D). One can also notice a strong attenuation accompanied by a slight shift toward the higher frequencies for line 5 associated with the surface DW mode for increasing dot diameter. Figure 3(c) compares the evolutions of the resonance frequency for the fundamental DW mode as a function of the dot diameter computed from micromagnetic simulations and from the domain model. In this last case, the small-amplitude DW dynamics is described by a harmonic oscillator equation,

$$m\frac{d^2q}{dt^2}+b\frac{dq}{dt}+kq=2M_S h_{rf,z}, \tag{8}$$

where q is the small radial DW displacement assumed independent of the z coordinate, $r_w=r_{w0}+q$, m is the DW mass, b is the viscous parameter, k is the restoring force constant, and $h_{rf,z}$ is the exciting magnetic field applied along the z axis. The angular resonance frequency ω_r is then given by

$$\omega_r=\sqrt{\frac{k}{m}}. \tag{9}$$

The mass per unit DW area is taken equal to the Döring mass, $m_D=(\mu_0\gamma^2\Delta_0/2)^{-1}$. The restoring force constant per unit DW area arises from to the static demagnetizing field and is defined as:[13] $k=\frac{1}{2\pi r_{w0}L_z}\frac{\partial^2 E_D}{\partial r_w^2}|_{r_w=r_{w0}}=\frac{1}{2\pi r_{w0}L_z}\times -2M_S\frac{\partial \bar{H}_{D,z}(r_w)}{\partial r_w}|_{r_w=r_{w0}}$, with E_D the demagnetizing energy of the dot. Using Eq. (6), the restoring force constant takes the following expression:

$$k=\frac{2\mu_0 M_S^2}{r_{w0}}\left\{\frac{4r_{w0}}{L_z}\left[F_1\left(1,\frac{L_z}{r_{w0}}\right)-F_1(1,0)\right]-\frac{2r}{L_z}\left[F_1\left(\frac{r}{r_{w0}},0\right)-F_1\left(\frac{r}{r_{w0}},\frac{L_z}{r_{w0}}\right)\right]-\frac{r^2}{r_{w0}L_z}\left[F_2\left(\frac{r}{r_{w0}},\frac{L_z}{r_{w0}}\right)-F_2\left(\frac{r}{r_{w0}},0\right)\right]+\frac{r}{r_{w0}}F_3\left(\frac{r}{r_{w0}},\frac{L_z}{r_{w0}}\right)-2F_3\left(1,\frac{L_z}{r_{w0}}\right)\right\}, \tag{10}$$

with $F_2(a,b)=\int_0^\infty e^{-bu}J_0(au)J_0(u)du$ and $F_3(a,b)=\int_0^\infty e^{-bu}J_0(u)J_1(au)du$.

As a result, both the micromagnetic simulations and the domain model predict a lowering of the resonance frequency for the fundamental DW mode as the dot radius increases for $r>70$ nm. Although the numerical and theoretical approaches lead to the same spectral range for the DW resonance, this one is overestimated by the domain model. This discrepancy could be partly attributed to the DW twist neglected in the domain model. The mixed Bloch-Néel character results in an increase in the DW mass.[13] For $r<70$ nm, the DW resonance frequency drops as the dot radius decreases for the domain model in contrast to the micromagnetic simulations. For the domain model, this behavior reflects the radius dependence of the restoring force constant, k passing through a maximum for $r\simeq 70$ nm. Similar evolutions have been reported for different magnetic systems (periodic stripe domains, isolated bubble in an infinite plate) with magnetostatic restoring forces arising from surface magnetic charges.[13] For 3D objects in the size range where the confinement effect becomes important, this approximation is too crude. The nonuniform magnetic configuration induces additional restoring forces (magnetostatic and exchange in nature), which should be taken into account. As a conclusion, the domain model seems appropriate for describing the static properties but cannot reproduce the dynamic behavior of the cylindrical DW in a large bubble radius range.

B. Tridomain bubble state

For larger dot diameters $D_0\geq 2$, a tridomain bubble state can be stabilized at remanence. An example of such a micromagnetic state is displayed in Fig. 1 (upper right image) for $D_0\simeq 2$. The tridomain bubble state consists in two up domains (inner and outer domains) and one intermediate down domain. These domains are separated by two circular DWs, the radial positions of which at the midplane of the dot are $r_{w0,1}=25.7$ nm and $r_{w0,2}=65.8$ nm, respectively. In contrast to the bidomain bubble states described in Sec. III A, the total magnetization along the symmetry axis is now positive, $\langle m_z\rangle=0.199$. For this dot diameter, the total magnetic energies associated with the bidomain and the tridomain bubble states are equivalent and equal to 3.0310^{-16} J. Beyond this value of diameter, the tridomain bubble structure becomes the ground state for the concentric domain configurations. The stability range of such a tridomain bubble state has been recently studied both experimentally and theoretically for FePt dots with a larger quality factor $Q=4.7$.[9] A higher value of the uniaxial anisotropy constant K_u (M_S being kept constant) induces an increase in the zero-field stripe period P_0. In this case, the existence of the tridomain bubble state is typically observed above $D=500$ nm, which corresponds also to $D_0\simeq 2$.

For the tridomain bubble state, it is interesting to distinguish two situations according to the relative chiralities of the DWs (the DW chirality is defined as the sense of rotation for the magnetization inside the DW). Let C_i be the chirality of the ith DW, $C_i=+1$ for counterclockwise rotation and $C_i=-1$ for clockwise rotation. Opposite and identical chiralities between the two DWs are characterized by $C_1C_2=-1$ and

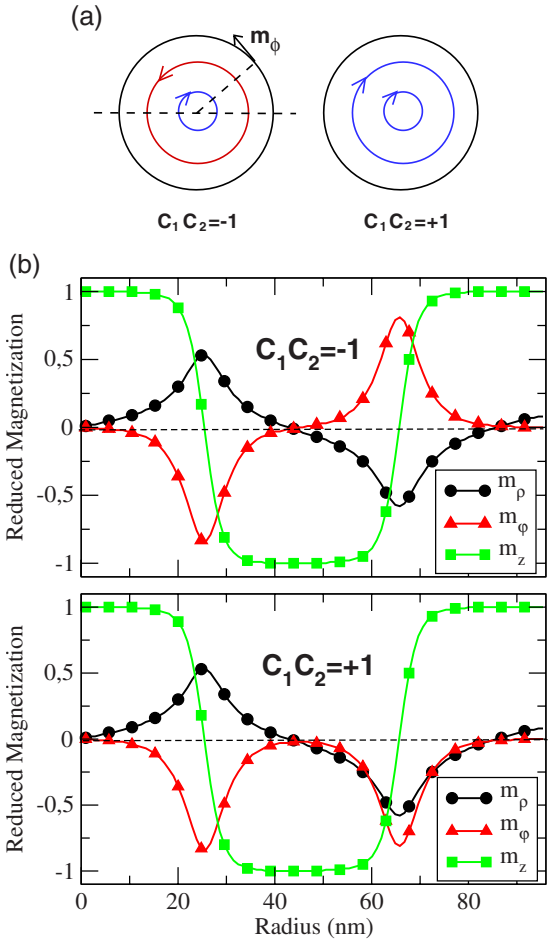

FIG. 4. (Color online) Static magnetization configurations for tridomain bubble states in a cylindrical dot with $Q=1.2$, $L_z=19.2$ nm, and $D=192$ nm. (a) Definition of relative DW chiralities. The arrows represent the sense of rotation for the magnetization within the DWs. (b) Magnetization profiles along the dot radius at the position $z=L_z/4$ for the tridomain bubble states with $C_1C_2=\pm 1$.

$C_1C_2=+1$, respectively [Fig. 4(a)]. The micromagnetic simulations yield the same total magnetic energies for both chirality configurations. The static magnetization profiles across the dot radius for the two types of tridomain bubble states are represented in Fig. 4(b). These profiles have been computed at the position $z=L_z/4$. Some striking features are revealed. (i) The magnetization is oriented along the symmetry axis inside the domain ($|\langle m_z\rangle|$ very close to unity). (ii) The azimuthal magnetization component m_φ is concentrated within the DWs. (iii) A significative radial magnetization component m_ρ exists also inside the DWs. This component passes through a maximum for $z=L_z/2$ (Néel-type DW) and disappears for $z=0$ (Bloch-type DW). The sign of m_ρ changes between the two DWs reflecting the opposite DW twists. (iv) At the middle of the intermediate domain, both azimuthal and radial magnetization components tend toward zero. This means that no overlapping exists between the two static DW profiles. (v) At the dot edge, a nonzero radial component of magnetization subsists due to the small flowering effect. This component vanishes at the midplane $z=0$

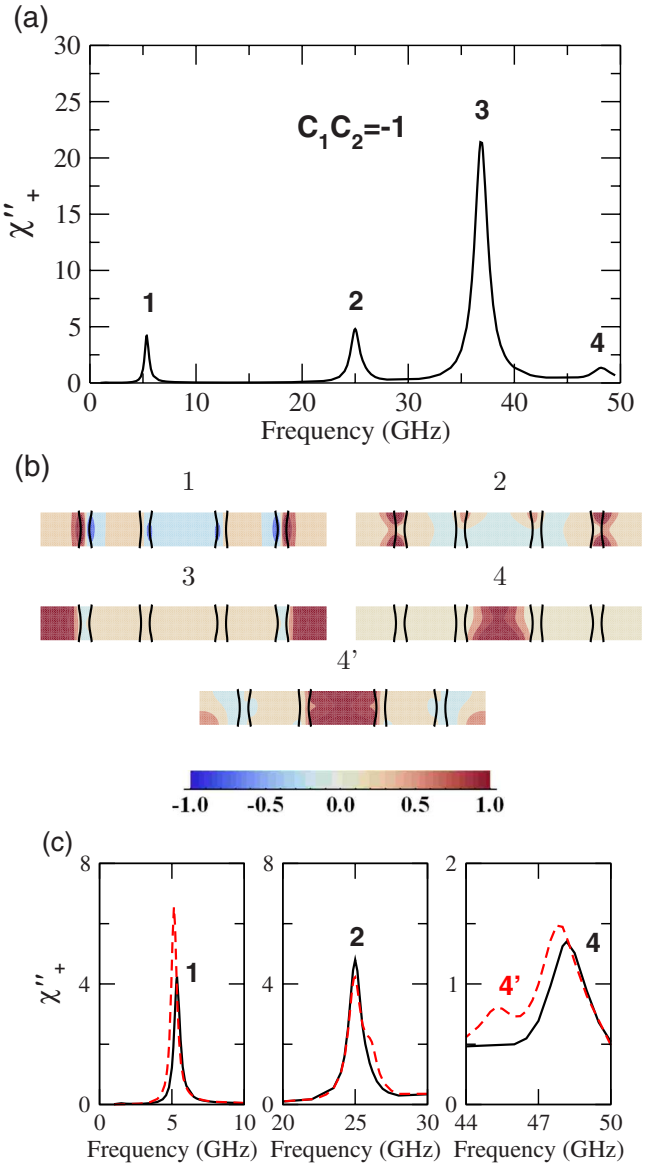

FIG. 5. (Color online) High-frequency response of the tridomain bubble state described in Fig. 4. (a) Zero-field dynamic susceptibility spectrum χ''_+ for $C_1C_2=-1$. (b) Cross-sectional view of local susceptibility in the vertical plane $y=0$ at the resonance frequency of different lines. The rule for color code imaging is the same as in Fig. 3. (c) Effect of the relative DW chiralities. The red dashed curves correspond to $C_1C_2=+1$, whereas the black solid lines are associated with $C_1C_2=-1$.

and takes its maximum value at the dot surfaces. For $z=L_z/4$, m_ρ is equal to 0.08 at the dot edge, and correlatively, due to the conservation of the magnetization modulus, m_z is slightly reduced, $m_z=0.997$. (vi) The two chirality configurations are only distinguished by the opposite signs of m_φ between the external DWs.

The high-frequency response of the tridomain bubble states is now investigated. First, the predominant circular dynamic susceptibility spectrum for the case $C_1C_2=-1$ is reported in Fig. 5(a). It should be noted that the opposite sign of $\langle m_z\rangle$ with respect to the bidomain bubble state results in change in the predominant circular polarization (χ_+ instead

of χ_-). The spectrum consists in four resonance lines. The positions of the three lowest-frequency lines (5.36, 24.99, and 36.86 GHz) are close to those obtained for the bidomain bubble state with $D=153.6$ nm (4.99, 25.05, and 35.73 GHz). A new excitation line appears at 48.17 GHz. The maps of local susceptibility [Fig. 5(b)] associated with lines 1, 2, and 3 resemble the ones described for the bidomain bubble state, namely, a mode localized at the lateral sides of the external DW, a surface mode concentrated near the external DW (up domain side), and a uniform domain mode within the external up domain. The external DW and the outer up domain for the tridomain bubble state play the role of the single DW, and the outer down domain for the bidomain bubble state. The new resonance line 4 is related to spins located inside the inner up domain with a significant inhomogeneity along the dot thickness. Figure 5(c) points out the effect of the relative DW chiralities on the χ''_+ spectrum. Transforming $C_1C_2=-1$ into $C_1C_2=+1$ (changing the chirality of the external DW) induces a shift of line 1 toward the low frequencies, appearance of a shouldering on the high-frequency side of line 2, and emergence of a new line labeled $4'$. The spatial distribution of mode $4'$ [Fig. 5(b)] indicates that it is mainly localized within the inner up domain but a significative response exists also within the outer up domain. In summary, inverting the relative chirality between the two DWs not only affects in a subtle way the absorption lines associated with the external DW, but also the one related to the inner domain far from the external DW. This demonstrates the existence of the dynamic magnetic coupling between the two DWs and between the domain and DW in such geometrical confined system. Regarding the dynamic coupling between domain and DW, it is worth noting that the intensive line 3 is not altered by the change in relative DW chirality (superimposition of lines 3 for $C_1C_2=\pm 1$, not presented here). The dynamic coupling between the two DWs is further highlighted when the pumping field is applied along the z axis. The χ''_{zz} spectrum is reported in Fig. 6(a) for the two types of tridomain bubble state. In each case, two resonance lines are observed within the frequency range 0.1–10 GHz instead of a unique peak for the bidomain bubble state. The resonance frequencies are $f_{r5}=2.81$ GHz and $f_{r6}=6.17$ GHz for $C_1C_2=-1$, and $f_{r5}=2.95$ GHz and $f_{r6}=5.88$ GHz for $C_1C_2=+1$. The map of local susceptibility for the two resonance lines is shown in Fig. 6(b) for the tridomain bubble state with $C_1C_2=-1$. The two lines result from coupled DW modes. For the low-frequency mode, the imaginary parts of the local susceptibility have opposite signs between the two DWs. This means that the two DWs oscillate out of phase along the radial direction (breathing DW mode). In contrast, the two DWs oscillate in phase along the radial direction for the high-frequency mode. It should be noted that for an infinite extent film with equivalent volumes of up and down domains, this mode would lead to a zero net magnetization along the z axis (displacement as a whole). For finite cylindrical dot and as a consequence of lateral geometrical confinement, the local susceptibility map indicates that the two DWs play an inequivalent role with a stronger dynamic response for the internal DW [Fig. 6(b)]. For the tridomain bubble state with $C_1C_2=+1$, the mode images appear quite similar. However, the spectral positions

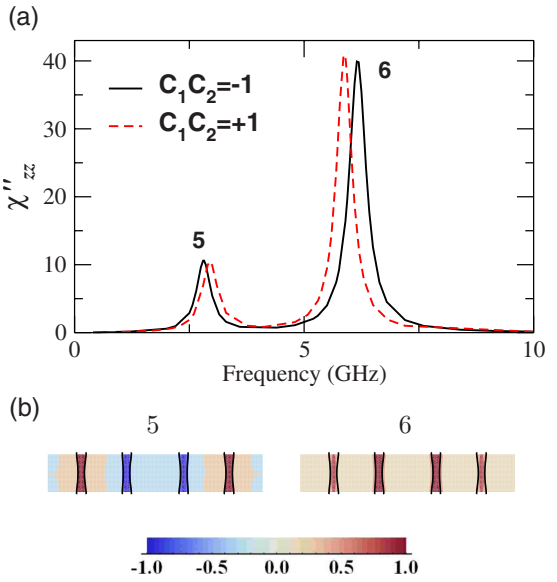

FIG. 6. (Color online) High-frequency response of the tridomain bubble state described in Fig. 4. (a) Zero-field dynamic susceptibility spectra χ''_{zz} for $C_1C_2=\pm 1$.(b) Cross-sectional view of local susceptibility in the vertical plane $y=0$ at the resonance frequency of the two lines for $C_1C_2=-1$. The rule for code color imaging is the same as in Fig. 3.

of resonance lines are shifted. The resonance frequency of line 1 increases, whereas the one of line 2 decreases. Furthermore, the product of resonance frequencies for each relative DW chirality is constant, $[f_{r5}\times f_{r6}]_{C_1C_2=-1}=[f_{r5}\times f_{r6}]_{C_1C_2=1}=17.34$ GHz^2. This kind of relationship has been also reported for the case of soft elliptical magnetic particles supporting a pair of magnetic vortices.[24] For this case, the topological quantity of interest is the polarization P_i of the ith vortex (direction of the magnetization inside the vortex core), $P_i=\pm 1$. As a result of the vortex-vortex dynamic interaction, four resonance modes resulting from the combination of the core polarization and the phase relation between the core motions have been predicted by micromagnetic simulations, and three of which have been experimentally detected using a broadband microwave reflection technique. More generally, the coupled DW dynamics inside the tridomain bubble state belongs to the up-to-date topic of soliton-pair dynamics including also, for instance, the vortex-antivortex interactions as recently reported.[25–27]

C. Metastable charged bidomain bubble state

The previous section has been devoted to axially symmetric micromagnetic states. However, some metastable states exist at remanence for high enough cylindrical dots. Let us consider a cylindrical dot with $D=153.6$ nm and $L_z=38.4$ nm. Starting from an initial magnetization configuration with an inner up domain surrounded by an outer down domain such as the net magnetization is zero along the z axis. The static micromagnetic simulations converge toward a bidomain bubble state including a pair of vertical BLs (charged bubble). In contrast, the same computation performed starting with an initial magnetic configuration with a

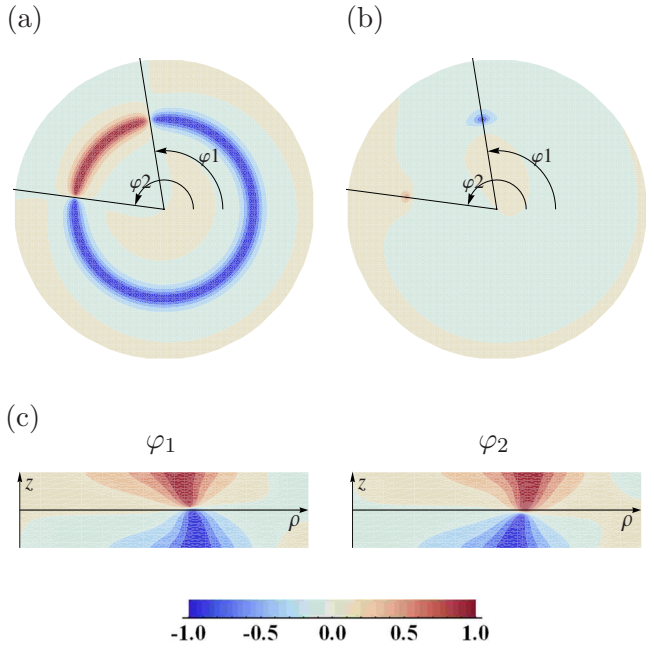

FIG. 7. (Color online) Static magnetization configuration for the charged bidomain bubble state with two BLs and two BPs. (a) Azimuthal magnetization component m_φ at the position $z=0$. (b) Radial magnetization component m_ρ at the position $z=0$. (c) Radial magnetization components in the vertical planes $\varphi=\varphi_1$ (left image) and $\varphi=\varphi_2$ (right image). The azimuthal and radial magnetization components are normalized by the saturation magnetization.

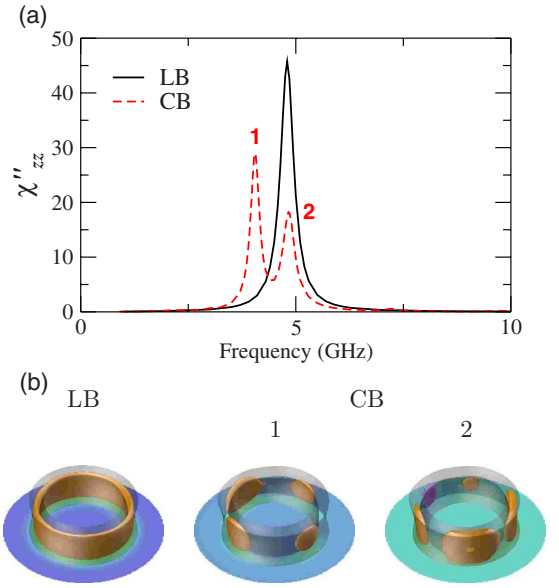

FIG. 8. (Color online) High-frequency responses for the light bubble (LB) and the charged bubble (CB) described in Fig. 7. (a) Zero-field dynamic susceptibility spectra χ''_{zz}. (b) Local susceptibility maps for the light and charged bidomain bubble states. The isosurfaces in beige correspond to the 5% highest positive values, the ones in purple to the 5% highest negative values.

net magnetization along the z axis approaching the real value results in an equilibrium bidomain bubble state without BLs (normal or light bubble). Surprisingly, the total magnetic energies of the light and charged bubbles are very close, 2.771×10^{-16} J and 2.796×10^{-16} J, respectively. A detailed analysis of the charged bubble state has been realized. Figure 7(a) shows the azimuthal magnetization component m_φ at the position $z=0$. The DW consists in two parts with positive and negative values of m_φ, respectively. The locations where $m_\varphi=0$ inside the DW determine the positions of BLs characterized by the azimuthal angles $\varphi_1=99.1°$ and $\varphi_2=172.3°$. Figure 7(b) represents the radial magnetization component m_ρ in the horizontal plane $z=0$. The BLs appear with opposite signs of m_ρ corresponding to opposite BL chiralities. In order to gain a better understanding of the BL structure, the maps of m_ρ in the two vertical planes $\varphi=\varphi_1$ and $\varphi=\varphi_2$ are displayed in Fig. 7(c). Some features are revealed. (i) The two BLs are canted in opposite senses with respect to the z axis. (ii) The sign of the radial magnetization component changes along the dot thickness revealing the existence of a BP within each BL. (iii) A detailed analysis evidences that the BPs possess symmetric z positions with respect to the midplane $z=0$. The BPs are located between the mesh nodes, and an estimate of their position is $z_{BP,1}\simeq-1.4$ nm$\simeq-z_{BP,2}$. As a consequence, the two BLs have the same chiralities for $z<z_{BP,1}$ and $z>z_{BP,2}$, and opposite chiralities for $z_{BP,1}<z<z_{BP,2}$. The different types of charged bubble states have been described in depth during the extensive works on bubble garnet films.[13] By adopting the classification used in Ref. 13, a bidomain bubble state can be characterized by the triplet (S,l,p), where S is the winding number, l is the number of BLs, and p is the number of BPs. Our charged bubble corresponds to a (1,2,2) state, whereas the light bidomain bubble is associated with a (1,0,0) state. Lastly, the question of asymmetric azimuthal positions of BLs within the DW has been discussed in the past.[28] This equilibrium spacing results from a balance between the magnetostatic and exchange interactions. A similar situation has been reported in ring elements supporting a twisted state including two interacting transverse DWs.[29]

Figure 8(a) shows the χ''_{zz} spectrum obtained for the light and charged bidomain bubbles. The presence of BLs induces a splitting of the initial unique resonance line into two peaks labeled 1 and 2 at 4.05 GHz and 4.83 GHz, respectively. For the light bubble, this line arises from the uniform DW mode. For the charged bubble, the two modes are localized within the DW, but only some parts of DW contribute to the dynamics. In particular, the BL regions are weakly excited. For mode 2, the DW region delimited by the BLs oscillates out of phase with respect to the other excited DW parts. It should be noted that a small-amplitude signal (about two orders of magnitude weaker with respect to resonance lines 1 and 2) has been also observed at 7.25 GHz (not presented here). This peak is assigned to a higher-order DW mode with multiple azimuthal nodes. In all cases, the presence of Bloch lines is indirectly revealed through the perturbation induced in the DW spectrum. No evidence of Bloch line resonances has been stated within the frequency range 1–10 GHz. The question of DW resonances in the presence of BLs and eventually BPs was addressed in the past both theoretically and experimentally for the case of bubble garnet films.[30–33] For an isolated magnetic bubble, it was demonstrated that the resonance frequency of the fundamental DW mode depends

on the DW state.[30] Moreover, a new coupled DW and BL mode localized at the BL position, the resonance frequency of which lies below the one of the fundamental DW breathing mode, has been predicted for a straight 180° DW with a vertical BL and evidenced using magneto-optic resonance spectroscopy.[32] In our case, the situation is quite different due to the complexity of the charged bubble state and the interaction between the two BLs. The coupled dynamics of DW and BL in this rigid magnetic structure is probably extensively modified, which could explain the absence of resonance lines associated with VBLs. The large value of the damping parameter (one order of magnitude larger than the one of garnet film reported in Ref. 32) could also screen the modes localized at the VBL positions. Nevertheless, the presence of magnetic singularities modifies significantly the high-frequency response of bidomain bubble states.

IV. SUMMARY AND CONCLUSIONS

The excitation spectrum of multidomain bubble states has been studied by means of 3D micromagnetic simulations. In such systems and for a fixed dot thickness, the relevant parameter is the dot diameter, which controls the number of domains. For the regime of diameter where the bidomain bubble is the ground state, increasing dot diameter results in a shift of the resonance frequencies for the main DW, and domain excitations toward the low frequencies. For a larger dot diameter where a tridomain bubble state can be stabilized, the high-frequency response of a tridomain state has been investigated. The dynamic susceptibility spectrum along the z axis exhibits two coupled DW modes (out-of-phase and in-phase DW oscillations along the radial direction), the resonance frequency of which depends on the relative DW chiralities. Lastly, a metastable bidomain bubble state including a pair of vertical BLs, each of them possessing a BP, has been also analyzed. As a result, such a complicated magnetic state modifies deeply the high-frequency spectrum with a splitting of the fundamental DW mode into multiple modes arising from oscillations of DW segments with different phase relations. This last finding provides an example of the impact of magnetic singularities on the dynamic susceptibility spectra. More generally, one can anticipate the expected complexity of dynamic susceptibility spectra for real dots due to the presence of geometrical irregularities or defects. Such remarks would have to be kept in mind for the applications based on bubble domain elements. Lastly, it would be crucial to compare our numerical findings with experimental data arising from broadband ferromagnetic resonance experiments. In particular, the intensive DW excitations lying at a few GHz could be detected in perpendicular pumping configuration (exciting field along the z axis).

ACKNOWLEDGMENTS

The authors acknowledge A. Thiaville for fruitful exchanges regarding the static properties of charged bidomain bubble states.

*nicolas.vukadinovic@dassault-aviation.fr

[1] M. Hehn, K. Ounadjela, J.-P. Bucher, F. Rousseaux, D. Decanini, B. Bartenlian, and C. Chappert, Science **272**, 1782 (1996).
[2] S. E. Russek and W. E. Bailey, IEEE Trans. Magn. **36**, 2990 (2000).
[3] P. Eames and E. D. Dahlberg, J. Appl. Phys. **91**, 7986 (2002).
[4] J. K. Ha, R. Hertel, and J. Kirschner, Europhys. Lett. **64**, 810 (2003).
[5] L. D. Buda, I. L. Prejbeanu, M. Demand, U. Ebels, and K. Ounadjela, Comput. Mater. Sci. **24**, 181 (2002).
[6] G. D. Skidmore, A. Kunz, C. E. Campbell, and E. D. Dahlberg, Phys. Rev. B **70**, 012410 (2004).
[7] C. Moutafis, S. Komineas, C. A. F. Vaz, J. A. C. Bland, and P. Eames, Phys. Rev. B **74**, 214406 (2006).
[8] S. Komineas, C. A. F. Vaz, J. A. C. Bland, and N. Papanicolaou, Phys. Rev. B **71**, 060405(R) (2005).
[9] C. Moutafis, S. Komineas, C. A. F. Vaz, J. A. C. Bland, T. Shima, T. Seki, and K. Takanashi, Phys. Rev. B **76**, 104426 (2007).
[10] C. Kooy and U. Enz, Philips Res. Rep. **15**, 7 (1960).
[11] For not too large Q values ($Q \simeq 1-2$), P_0 is generally computed by static micromagnetic simulations. Nevertheless, the theory of domains provides a good estimate of P_0 by solving numerically the following equation (Ref. 10): $\frac{l}{L_z} = -\frac{2\mu}{\pi^3\beta}\sum_{\text{nodd}}^{\infty}\frac{1}{n^3}\left[\frac{n\pi\sqrt{\mu}}{B^2} - \frac{\sinh(n\pi\beta)}{\beta B}\right]$, with $l = \frac{4\sqrt{AK_u}}{\mu_0 M_S^2}$, $\mu = 1 + \frac{1}{Q}$, $\beta = \frac{L_z\sqrt{\mu}}{P_0}$, $B = \sinh(n\pi\beta) + \sqrt{\mu}\cosh(n\pi\beta)$, L_z is the film thickness, and A is the exchange constant.
[12] A. Hubert and R. Schaeffer, *Magnetic Domains* (Springer, Heidelberg, 1998).
[13] A. P. Malozemoff and J. C. Slonczewski, *Magnetic Domain Walls in Bubble Materials* (Academic, New York, 1979).
[14] N. Vukadinovic and F. Boust, Phys. Rev. B **75**, 014420 (2007).
[15] S. Labbé and P. Y. Bertin, J. Magn. Magn. Mater. **206**, 93 (1999).
[16] N. Vukadinovic, O. Vacus, M. Labrune, O. Acher, and D. Pain, Phys. Rev. Lett. **85**, 2817 (2000).
[17] F. Boust and N. Vukadinovic, Phys. Rev. B **70**, 172408 (2004).
[18] A. A. Thiele, Bell Syst. Tech. J. **48**, 3287 (1969).
[19] W. F. Druyvesteyn, R. Szymczak, and R. Wadas, Phys. Status Solidi A **9**, 343 (1972).
[20] R. I. Joseph and E. Schloemann, J. Appl. Phys. **36**, 1579 (1965).
[21] W. F. Druyvesteyn and F. A. de Jonge, Philips Res. Rep. **25**, 415 (1970).
[22] N. Vukadinovic, J. Ben Youssef, and M. Labrune, Phys. Rev. B **66**, 132418 (2002).
[23] M. Yan, R. Hertel, and C. M. Schneider, Phys. Rev. B **76**, 094407 (2007).
[24] K. S. Buchanan, P. E. Roy, M. Grimsditch, F. Y. Fradin, K. Y. Guslienko, S. Bader, and V. Novosad, Nat. Phys. **1**, 172 (2005).
[25] R. Hertel and C. M. Schneider, Phys. Rev. Lett. **97**, 177202 (2006).
[26] S. Komineas, Phys. Rev. Lett. **99**, 117202 (2007).
[27] K. Kuepper, M. Buess, J. Raabe, C. Quitmann, and J. Fass-

bender, Phys. Rev. Lett. **99**, 167202 (2007).
[28] T. H. O'Dell, *Ferromagnetodynamics* (Macmillan, London, 1981).
[29] F. J. Castano, C. A. Ross, C. Frandsen, A. Eilez, D. Gil, H. I. Smith, M. Redjdal, and F. B. Humphrey, Phys. Rev. B **67**, 184425 (2003).
[30] W. Jantz, J. C. Slonczewski, and B. E. Argyle, J. Magn. Magn. Mater. **23**, 8 (1981).
[31] V. L. Dorman, V. L. Sobolev, and A. B. Shevchenko, J. Magn. Magn. Mater. **94**, 293 (1991).
[32] J. Jalishev, V. Pokazan'ev, I. Jeberlaev, K. Lukash, and O. Troshin, J. Magn. Magn. Mater. **102**, 208 (1991).
[33] V. L. Dorman, V. L. Sobolev, and A. B. Shevchenko, J. Magn. Magn. Mater. **124**, 221 (1993).